Biomedical Optics EXPRESS

Multi-modal adaptive optics system including fundus photography and optical coherence tomography for the clinical setting

Matthias Salas,[1,*] Wolfgang Drexler,[1] Xavier Levecq,[2] Barbara Lamory,[2] Markus Ritter,[3] Sonja Prager,[3] Julia Hafner,[3] Ursula Schmidt-Erfurth,[3] and Michael Pircher[1]

[1]*Center of Medical Physics and Biomedical Engineering, Medical University of Vienna, Waehringer Guertel 18-20 A-1090 Vienna, Austria*

[2]*Imagine Eyes, 18 Rue Charles de Gaulle 91400 Orsay, France*

[3]*Department of Ophthalmology and Optometry, Medical University of Vienna, Waehringer Guertel 18-20 A-1090 Vienna, Austria*

[*]*Matthias.salas@meduniwien.ac.at*

Abstract: We present a new compact multi-modal imaging prototype that combines an adaptive optics (AO) fundus camera with AO-optical coherence tomography (OCT) in a single instrument. The prototype allows acquiring AO fundus images with a field of view of 4°x4° and with a frame rate of 10fps. The exposure time of a single image is 10 ms. The short exposure time results in nearly motion artifact-free high resolution images of the retina. The AO-OCT mode allows acquiring volumetric data of the retina at 200kHz A-scan rate with a transverse resolution of ~4 µm and an axial resolution of ~5 µm. OCT imaging is acquired within a field of view of 2°x2° located at the central part of the AO fundus image. Recording of OCT volume data takes 0.8 seconds. The performance of the new system is tested in healthy volunteers and patients with retinal diseases.

OCIS codes: (170.3890) Medical optics instrumentation; (170.4470) Ophthalmology; (110.1080) Active or adaptive optics; (110.4500) Optical coherence tomography.

References and links

1. A. F. Fercher, C. K. Hitzenberger, G. Kamp, and S. Y. El-Zaiat, "Measurement of intraocular distances by backscattering spectral interferometry," Opt. Commun. **117**(1-2), 43–48 (1995).
2. M. Wojtkowski, R. Leitgeb, A. Kowalczyk, T. Bajraszewski, and A. F. Fercher, "In vivo human retinal imaging by Fourier domain optical coherence tomography," J. Biomed. Opt. **7**(3), 457–463 (2002).
3. N. Nassif, B. Cense, B. Park, M. Pierce, S. Yun, B. Bouma, G. Tearney, T. Chen, and J. de Boer, "In vivo high-resolution video-rate spectral-domain optical coherence tomography of the human retina and optic nerve," Opt. Express **12**(3), 367–376 (2004).
4. M. E. J. van Velthoven, D. J. Faber, F. D. Verbraak, T. G. van Leeuwen, and M. D. de Smet, "Recent developments in optical coherence tomography for imaging the retina," Prog. Retin. Eye Res. **26**(1), 57–77 (2007).
5. W. Drexler and J. G. Fujimoto, "State-of-the-art retinal optical coherence tomography," Prog. Retin. Eye Res. **27**(1), 45–88 (2008).
6. W. Geitzenauer, C. K. Hitzenberger, and U. M. Schmidt-Erfurth, "Retinal optical coherence tomography: past, present and future perspectives," Br. J. Ophthalmol. **95**(2), 171–177 (2011).
7. A. F. Fercher and E. Roth, "Ophthalmic Laser Interferometry," Proc. SPIE **658**, 48–51 (1986).
8. D. Huang, E. A. Swanson, C. P. Lin, J. S. Schuman, W. G. Stinson, W. Chang, M. R. Hee, T. Flotte, K. Gregory, C. A. Puliafito, and J. G. Fujimoto, "Optical coherence tomography," Science **254**(5035), 1178–1181 (1991).
9. H. Hofer, P. Artal, B. Singer, J. L. Aragón, and D. R. Williams, "Dynamics of the eye's wave aberration," J. Opt. Soc. Am. A **18**(3), 497–506 (2001).
10. J. Porter, A. Guirao, I. G. Cox, and D. R. Williams, "Monochromatic aberrations of the human eye in a large population," J. Opt. Soc. Am. A **18**(8), 1793–1803 (2001).
11. J. Liang and D. R. Williams, "Aberrations and retinal image quality of the normal human eye," J. Opt. Soc. Am. A **14**(11), 2873–2883 (1997).

#258577 Received 29 Jan 2016; revised 21 Mar 2016; accepted 1 Apr 2016; published 11 Apr 2016

12. H. Babcock, "The Possibility of Compensating Astronomical Seeing," Publ. Astron. Soc. Pac. **65**, 229–236 (1953).
13. J. W. Hardy, J. Feinleib, and J. C. Wyant, "Real time phase correction of optical imaging systems," in Topical Meeting on Optical Propagation through Turbulence 1974.
14. J. Liang, D. R. Williams, and D. T. Miller, "Supernormal vision and high-resolution retinal imaging through adaptive optics," J. Opt. Soc. Am. A **14**(11), 2884–2892 (1997).
15. A. Roorda, F. Romero-Borja, W. Donnelly III, H. Queener, T. Hebert, and M. Campbell, "Adaptive optics scanning laser ophthalmoscopy," Opt. Express **10**(9), 405–412 (2002).
16. D. T. Miller, J. Qu, R. S. Jonnal, and K. E. Thorn, "Coherence gating and adaptive optics in the eye," Proc. SPIE **456**, 65–72 (2003).
17. M. Mujat, R. D. Ferguson, N. Iftimia, and D. X. Hammer, "Compact adaptive optics line scanning ophthalmoscope," Opt. Express **17**(12), 10242–10258 (2009).
18. A. Roorda, "Adaptive optics for studying visual function: A comprehensive review," J. Vis. **11**(7), doi:10.1167/11.5.6 (2011).
19. M. Lombardo, S. Serrao, N. Devaney, M. Parravano, and G. Lombardo, "Adaptive Optics Technology for High-Resolution Retinal Imaging," Sensors (Basel) **13**(1), 334–366 (2012).
20. B. Hermann, E. J. Fernández, A. Unterhuber, H. Sattmann, A. F. Fercher, W. Drexler, P. M. Prieto, and P. Artal, "Adaptive-optics ultrahigh-resolution optical coherence tomography," Opt. Lett. **29**(18), 2142–2144 (2004).
21. E. J. Fernández, B. Považay, B. Hermann, A. Unterhuber, H. Sattmann, P. M. Prieto, R. Leitgeb, P. Ahnelt, P. Artal, and W. Drexler, "Three-dimensional adaptive optics ultrahigh-resolution optical coherence tomography using a liquid crystal spatial light modulator," Vision Res. **45**(28), 3432–3444 (2005).
22. R. J. Zawadzki, S. M. Jones, S. S. Olivier, M. Zhao, B. A. Bower, J. A. Izatt, S. Choi, S. Laut, and J. S. Werner, "Adaptive-optics optical coherence tomography for high-resolution and high-speed 3D retinal in vivo imaging," Opt. Express **13**(21), 8532–8546 (2005).
23. Y. Zhang, J. Rha, R. Jonnal, and D. Miller, "Adaptive optics parallel spectral domain optical coherence tomography for imaging the living retina," Opt. Express **13**(12), 4792–4811 (2005).
24. M. Pircher, R. J. Zawadzki, J. W. Evans, J. S. Werner, and C. K. Hitzenberger, "Simultaneous imaging of human cone mosaic with adaptive optics enhanced scanning laser ophthalmoscopy and high-speed transversal scanning optical coherence tomography," Opt. Lett. **33**(1), 22–24 (2008).
25. D. Merino, C. Dainty, A. Bradu, and A. G. Podoleanu, "Adaptive optics enhanced simultaneous en-face optical coherence tomography and scanning laser ophthalmoscopy," Opt. Express **14**(8), 3345–3353 (2006).
26. M. Pircher and R. Zawadzki, "Combining adaptive optics with optical coherence tomography: Unveiling the cellular structure of the human retina in vivo," Exp. Rev. Ophthalmol. **2**, 16 (2007).
27. F. Felberer, J. S. Kroisamer, B. Baumann, S. Zotter, U. Schmidt-Erfurth, C. K. Hitzenberger, and M. Pircher, "Adaptive optics SLO/OCT for 3D imaging of human photoreceptors in vivo," Biomed. Opt. Express **5**(2), 439–456 (2014).
28. F. Felberer, M. Rechenmacher, R. Haindl, B. Baumann, C. K. Hitzenberger, and M. Pircher, "Imaging of retinal vasculature using adaptive optics SLO/OCT," Biomed. Opt. Express **6**(4), 1407–1418 (2015).
29. J. Carroll, D. B. Kay, D. Scoles, A. Dubra, and M. Lombardo, "Adaptive Optics Retinal Imaging - Clinical Opportunities and Challenges," Curr. Eye Res. **38**(7), 709–721 (2013).
30. D. A. Robinson, "The mechanics of human saccadic eye movement," J. Physiol. **174**(2), 245–264 (1964).
31. R. J. Zawadzki, A. G. Capps, D. Y. Kim, A. Panorgias, S. B. Stevenson, B. Hamann, and J. S. Werner, "Progress on Developing Adaptive Optics–Optical Coherence Tomography for In Vivo Retinal Imaging: Monitoring and Correction of Eye Motion Artifacts," IEEE J. Sel. Top.Quantum Electron. **20**, 7100912 (2014).
32. O. P. Kocaoglu, R. D. Ferguson, R. S. Jonnal, Z. Liu, Q. Wang, D. X. Hammer, and D. T. Miller, "Adaptive optics optical coherence tomography with dynamic retinal tracking," Biomed. Opt. Express **5**(7), 2262–2284 (2014).
33. O. P. Kocaoglu, T. L. Turner, Z. Liu, and D. T. Miller, "Adaptive optics optical coherence tomography at 1 MHz," Biomed. Opt. Express **5**(12), 4186–4200 (2014).
34. M. Lombardo, S. Serrao, P. Ducoli, and G. Lombardo, "Eccentricity dependent changes of density, spacing and packing arrangement of parafoveal cones," Ophthalmic Physiol. Opt. **33**(4), 516–526 (2013).
35. M. Mujat, A. Patel, N. Iftimia, and R. D. Ferguson, "Compact adaptive optics line scanning retinal imager; closer to the clinic," Proc. SPIE **89301**, 89301B (2014).
36. A. Meadway, X. Wang, C. A. Curcio, and Y. Zhang, "Microstructure of subretinal drusenoid deposits revealed by adaptive optics imaging," Biomed. Opt. Express **5**(3), 713–727 (2014).
37. S. Mrejen, T. Sato, C. A. Curcio, and R. F. Spaide, "Assessing the cone photoreceptor mosaic in eyes with pseudodrusen and soft drusen in vivo using adaptive optics imaging," Ophthalmology **121**(2), 545–551 (2014).
38. D. X. Hammer, N. V. Iftimia, R. D. Ferguson, C. E. Bigelow, T. E. Ustun, A. M. Barnaby, and A. B. Fulton, "Foveal Fine Structure in Retinopathy of Prematurity: An Adaptive Optics Fourier Domain Optical Coherence Tomography Study," Invest. Ophthalmol. Vis. Sci. **49**(5), 2061–2070 (2008).
39. J. G. Cunha-Vaz, "Pathophysiology of diabetic retinopathy," Br. J. Ophthalmol. **62**(6), 351–355 (1978).
40. M. Dubow, A. Pinhas, N. Shah, R. F. Cooper, A. Gan, R. C. Gentile, V. Hendrix, Y. N. Sulai, J. Carroll, T. Y. P. Chui, J. B. Walsh, R. Weitz, A. Dubra, and R. B. Rosen, "Classification of Human Retinal Microaneurysms Using Adaptive Optics Scanning Light Ophthalmoscope Fluorescein Angiography," Invest. Ophthalmol. Vis. Sci. **55**(3), 1299–1309 (2014).

#258577 Received 29 Jan 2016; revised 21 Mar 2016; accepted 1 Apr 2016; published 11 Apr 2016

41. M. Lombardo, M. Parravano, S. Serrao, P. Ducoli, M. Stirpe, and G. Lombardo, "Analysis of retinal capillaries in patients with type 1 diabetes and nonproliferative diabetic retinopathy using adaptive optics imaging," Retina **33**(8), 1630–1639 (2013).
42. E. Lieth, T. W. Gardner, A. J. Barber, and D. A. Antonetti; Penn State Retina Research Group, "Retinal neurodegeneration: early pathology in diabetes," Clin. Experiment. Ophthalmol. **28**(1), 3–8 (2000).
43. J. K. Sun, S. Prager, S. Radwan, D. J. Ramsey, P. S. Silva, H. Kwak, S. A. Burns, and L. P. Aiello, "Photoreceptor Mosaic Changes in Diabetic Eye Disease Assessed by Adaptive Optics Scanning Laser Ophthalmoscopy (AOSLO)," Invest. Ophthalmol. Vis. Sci. **53**, 4647 (2012).
44. M. Parravano, M. Lombardo, G. Lombardo, B. Boccassini, S. Lioi, and M. Varano, "In Vivo Investigation of the Retinal Microscopy in Patients with Type 1 Diabetes Mellitus," Invest. Ophthalmol. Vis. Sci. **53**, 5657 (2012).
45. A. Boretsky, F. Khan, G. Burnett, D. X. Hammer, R. D. Ferguson, F. van Kuijk, and M. Motamedi, "In vivo imaging of photoreceptor disruption associated with age-related macular degeneration: A pilot study," Lasers Surg. Med. **44**(8), 603–610 (2012).
46. F. Felberer, J.-S. Kroisamer, C. K. Hitzenberger, and M. Pircher, "Lens based adaptive optics scanning laser ophthalmoscope," Opt. Express **20**(16), 17297–17310 (2012).
47. C. Viard, K. Nakashima, B. Lamory, M. Pâques, X. Levecq, and N. Château, "Imaging microscopic structures in pathological retinas using a flood-illumination adaptive optics retinal camera," Proc. SPIE **7885**, 788509 (2011).
48. M. Pircher and R. J. Zawadzki, "Combining adaptive optics with optical coherence tomography: unveiling the cellular structure of the human retina in vivo," Expert Rev. Ophthalmol. **2**(6), 1019 (2007).
49. I. E. C. (IEC), "Safety of laser products," in *IEC 60825–1* (3rd edition 2014).
50. C. Kulcsár, G. Le Besnerais, E. Ödlund, and X. Lévecq, "Robust processing of images sequences produced by an adaptive optics retinal camera," in *Img. and Appl. Opt.*, OSA Technical Digest (2013)
51. C. Kulcs, E. R. Fezzani, G. L. Besnerais, A. Plyer, and X. Levecq, "Fast and robust image registration with local motion estimation for image enhancement and activity detection in retinal imaging," *Comp. Intell. for Multim. Underst. (IWCIM), 2014 Internat. Workshopn*,, 1–5 (2014).
52. R. S. Jonnal, O. P. Kocaoglu, R. J. Zawadzki, S. H. Lee, J. S. Werner, and D. T. Miller, "The Cellular Origins of the Outer Retinal Bands in Optical Coherence Tomography Images," Invest. Ophthalmol. Vis. Sci. **55**(12), 7904–7918 (2014).
53. M. Pircher, J. S. Kroisamer, F. Felberer, H. Sattmann, E. Götzinger, and C. K. Hitzenberger, "Temporal changes of human cone photoreceptors observed in vivo with SLO/OCT," Biomed. Opt. Express **2**(1), 100–112 (2011).
54. C. E. Pang, Y. Suqin, J. Sherman, and K. B. Freund, "New Insights Into Stargardt Disease With Multimodal Imaging," Ophthalmic Surg. Lasers Imaging Retina **46**(2), 257–261 (2015).
55. M. A. Reback, H. X. Song, L. R. Latchney, and M. M. Chung, "Longitudinal adaptive optics imaging reveals regional variation in cone and rod loss in Stargardt disease," Invest. Ophthalmol. Vis. Sci. **56**, 4929 (2015).
56. H. Song, E. A. Rossi, L. Latchney, A. Bessette, E. Stone, J. J. Hunter, D. R. Williams, and M. Chung, "Cone and Rod Loss in Stargardt Disease Revealed by Adaptive Optics Scanning Light Ophthalmoscopy," JAMA Ophthalmol. **133**(10), 1198–1203 (2015).
57. S. A. Burns, A. E. Elsner, T. Y. Chui, D. A. Vannasdale, Jr., C. A. Clark, T. J. Gast, V. E. Malinovsky, and A. D. T. Phan, "In vivo adaptive optics microvascular imaging in diabetic patients without clinically severe diabetic retinopathy," Biomed. Opt. Express **5**(3), 961–974 (2014).
58. M. Dubow, A. Pinhas, N. Shah, R. F. Cooper, A. Gan, R. C. Gentile, V. Hendrix, Y. N. Sulai, J. Carroll, T. Y. P. Chui, J. B. Walsh, R. Weitz, A. Dubra, and R. B. Rosen, "Classification of Human Retinal Microaneurysms Using Adaptive Optics Scanning Light Ophthalmoscope Fluorescein Angiography," Invest. Ophthalmol. Vis. Sci. **55**(3), 1299–1309 (2014).
59. R. J. Zawadzki, S. M. Jones, S. Pilli, S. Balderas-Mata, D. Y. Kim, S. S. Olivier, and J. S. Werner, "Integrated adaptive optics optical coherence tomography and adaptive optics scanning laser ophthalmoscope system for simultaneous cellular resolution in vivo retinal imaging," Biomed. Opt. Express **2**(6), 1674–1686 (2011).

1. Introduction

Spectral domain optical coherence tomography (SD-OCT) [1–3] is a well-established imaging technique that allows recording of cross sectional image data with unprecedented high axial resolution. Meanwhile the technique has been commercialized by several companies with its main impact in the field of ophthalmology [4–6].

Since the first proof of principle of the fundamental concept [7] and the first demonstration of its imaging capabilities [8], OCT technology has evolved rapidly in terms of speed and resolution. However, one limitation of OCT for retinal imaging is the rather low transverse resolution, insufficient to visualize discrete structures as individual cells. The human eye is an important optical system but in many cases the optical components of the eye introduce aberrations, resulting in an optical quality that is far from perfect [9, 10]. These aberrations become more pronounced with increasing beam diameter [11]. Thus instead of improving the image resolution by increasing the beam diameter these aberrations will lead to

#258577 Received 29 Jan 2016; revised 21 Mar 2016; accepted 1 Apr 2016; published 11 Apr 2016

a blurring of the image associated with a decrease in transverse resolution. To overcome this problem adaptive optics (AO), a technology originally intended for astronomy [12] and powered by military purposes [13] has been successfully coupled with different retinal imaging techniques [14–17]. AO measures and corrects wavefront aberrations introduced by the eye in real time enabling a diffraction limited spot at the retina even in the case of large beam diameters [18, 19]. Especially the combination of AO with OCT (AO-OCT) has enabled high isotropic retinal image resolution and enabled the visualization of three dimensional cellular structures of the retina in-vivo [16, 20–28].

Apart from the exciting performance that AO-OCT has already demonstrated, the real clinical value of this imaging technique has not yet been translated to the clinic [29]. Eye motion [30], low sensitivity, system complexity, high cost of the equipment, space requirements and the need of highly trained personnel are some of the obstacles that currently prevent an easy translation of this technology to the clinic. In order to address the problem of image artifacts caused by eye motion, retinal trackers [31, 32] and high speed AO-OCT imaging have been introduced [33]. The performance of such devices/techniques seems to be promising but they are still under development and they add additional cost and complexity to the instrument.

Meanwhile commercial AO devices are available that are based on AO-fundus camera [34] or combine AO-SLO and AO-SD-OCT in a single instrument [35]. The image quality and image resolution that could be achieved in patients has shown a promising advantage of this technology compared to instruments without AO assistance. These high-resolution images already aid our understanding and treatment of various retinal pathologies [36–38].

An example of such pathology is chronic hyperglycemia. The disease is usually caused by diabetes mellitus and frequently leads to diabetic retinopathy (DR), consisting of a microangiopathy that induces pathological changes of the vascular structures and the blood rheological properties [39]. AO technology coupled with SLO has demonstrated a useful opportunity to image retinal microvascular damage in DM patients, without the need of any contrast agent. Some of these lesions are: microaneurysms [40], increased foveal avascular zone (FAZ) size and dropout of capillaries at the edge of the FAZ [41]. Moreover, it has been postulated that DR is a multifactorial disease involving neuronal cells in the retina [42]. This disease has already been investigated with AO technology [43, 44] giving insight into the disease pathomorphology at a cellular level. Of course, microvasculature can also be imaged with AO-OCT and first images are quite promising [38]. Finally AO technology has shown potential to be also useful in age-related macular degeneration (AMD) by monitoring drusen over time and identifying small drusen that cannot be detected with state of the art technologies such as wide field fundus imaging or SD-OCT [45].

In this paper we present the design and results of a new prototype that combines an AO-fundus camera with an AO-SD-OCT system in a compact and easy to use platform. The aim of this work is to develop an AO-OCT instrument that is capable of achieving decent image quality in a large patient population. The relay optics of the AO system is entirely based on lenses [46], which allows a very compact design. The AO-fundus camera is based on a commercial product (RTX1, Orsay, France) [47]. Both imaging modalities share the same AO correction path and switching between the imaging modalities is currently achieved in series through a manually flip-able mirror. The performance of the instrument has been tested in several healthy volunteer and in patients with Stargardt disease and diabetic retinopathy.

2. Materials and methods

2.1 Optical system

The new prototype consists of two imaging modalities: AO-fundus photography (RTX1) and AO-OCT. In order to reduce size and costs, a major part of the imaging optics of the AO-fundus imager is used for the AO-OCT sample arm. A scheme of the setup is shown in Fig. 1.

#258577 Received 29 Jan 2016; revised 21 Mar 2016; accepted 1 Apr 2016; published 11 Apr 2016

AO correction needs wavefront sensing and corresponding wavefront modulation using a correcting device. In this system a separate laser beacon at a wavelength that differs from the imaging wavelengths (superluminescent diode EXS-7505-8411, Exalos, Schlieren, Switzerland at 750nm central wavelength) was used for wavefront sensing. The beacon (orange beam in Fig. 1) is coupled into the main system via a dichroic mirror and a semi-transparent beam splitter (70:30 splitting ratio, 30% of the light is directed to the eye). The light that is backscattered from the retina is imaged onto the deformable mirror (DM) with 52 elements (Mirao52-e RC, Imagine Eyes, Orsay, France) and onto the Shack-Hartman (SH) wavefront sensor (Haso first, Imagine Optics, Orsay, France) using lens based telescopes. The AO loop is run in closed loop mode with a loop time of ~66 milliseconds (15Hz). For AO-fundus imaging, the retina is illuminated using a light emitting diode at 850nm (LED, SFH 4235, OSRAM, Munich, Germany) that is coupled into the system using the semi-transparent mirror right before the eye. An extended illumination of the retina assembling a square of ~4 degrees side lengths is produced. The light that is backscattered from the retina is imaged (using the same imaging optics as for the laser beacon) onto the DM for wavefront correction. In order to adapt for defocus the first telescope is arranged in a Badal configuration. The light for wavefront sensing and retinal imaging is separated by a dichroic mirror that is placed before the second lens of the telescope that images the DM onto the SH sensor. The CCD camera (CoolsnapEZ, Roper Scientific, Planegg, Germany) for retinal imaging is placed in the focus of the first lens of this telescope which is the conjugated plane to the retinal plane. The exposure time of the camera was set to 10ms which greatly reduces image artifacts that are caused by eye motion. However, the rather long read out time of the camera results in a frame rate of 10fps. The field of view of the AO-fundus camera is 4°x4°.

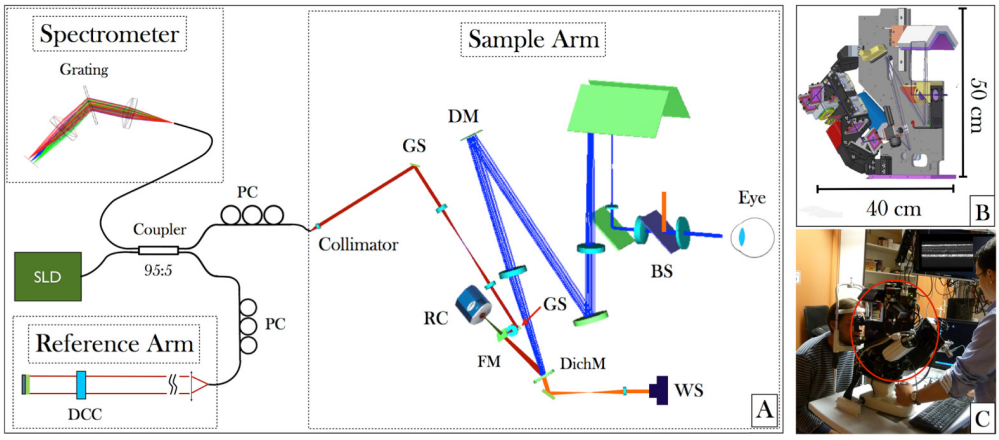

Fig. 1. (A) Layout of a Zemax simulation of the sample arm and schematic diagram of the AO-SD-OCT, showing the main components such as Galvanometer Scanners (GS), Retinal Camera (RC), Flip able mirror (FM), Dichroic mirror (DichM), Beam splitter (BS) and wavefront sensor (WS). (B) CAD picture of the mechanical design (C) Picture of the compact AO-fundus camera/AO-OCT instrument during operation at the laboratory (The AO scan head is entirely confined within the red ellipse and can be moved in three dimensions).

To facilitate easy patient alignment the instrument can be moved in three dimensions in respect to the patient's eye. To aid the alignment process an anterior segment camera (Guppy F033, Allied Vision, Stadtroda, Germany) is used in combination with a proper illumination of this part of the eye using light emitting diodes at 950 nm central wavelength (SFH 4511, OSRAM, Munich, Germany). Subject fixation is enabled through an internal fixation target that is coupled into the beam path of the system using dichroic mirrors.

The AO-OCT system consists of a fiber-based Michelson interferometer. The interferometer is illuminated with a superluminescent diode (S-840-B-I-20, Superlum, Cork,

#258577 Received 29 Jan 2016; revised 21 Mar 2016; accepted 1 Apr 2016; published 11 Apr 2016

Ireland) with a center wavelength of 841nm, a bandwidth of ~50nm and 33mW output power. The spectral bandwidth results in a theoretical axial resolution in the retina of ~5 µm (assuming a refractive index of 1.4) [48]. Light coming from the light source is split into sample and reference beam using a 95:5 coupler (Wavelength Flattened Coupler, Gould, Millersville, USA) where 5% of the light is directed to the sample arm. In the sample arm the light is collimated and directed to the x-y-scanning unit consisting of two galvanometer scanners (6210HM40, Cambridge Technology, Bedford, USA). The pivot point of the first scanner (x-direction) is imaged onto the pivot point of the second scanner (y-direction) using a lens-based telescope (cf. Fig. 1). The OCT beam is coupled into the beam path of the AO-fundus camera using a flip-able mirror. Using this mirror an easy switching between the AO-fundus and AO-OCT imaging modality is achieved. Before the flip-able mirror a lens is placed that acts together with the lens before the DM as telescope in order to image the pivot points of the scanning mirrors onto the DM. The beam size at the sample arm entrance of the AO-OCT system is 3 mm and is increased through the second telescope in the sample arm to 15 mm at the location of the DM. The telescope between DM and eye de-magnifies the beam diameter to ~5 mm at the eye. This yields a diffraction limited transverse resolution of ~4 µm at the retina [48]. The components of the sample arm are mounted on the same base mount as the AO-fundus camera as is shown in Fig. 1(B).

The optical power used for the measurements was 500 µW at 841 nm for the OCT imaging beam and 50 µW at 750 nm for the guide star. AO-fundus imaging was done with an extended retinal illumination of 1.1 mW at 850 nm. The combined light power of the OCT imaging beam and the guide star or the flood illumination and the guide star were below the limits for safe exposure according to the European standards [49].

The light that is directed to the reference arm of the interferometer traverses glass plates for dispersion compensation and is reflected by the reference arm mirror. The mirror is mounted on a translation stage, which allows for adapting the reference arm length. A variable neutral density filter is placed into the beam path, which allows for a precise adjustment of the light power returning from the reference arm. The power is set close to the saturation limit of the camera in the detection arm. The beams returning from sample and reference arm are brought to interference in the fiber coupler and the light is directed to the detection unit. To improve the fringe contrast, polarization paddles are used to match the polarization state of the light returning from the sample and reference arm, respectively. The detection unit is a custom made spectrometer consisting of a grating (1200 l/mm at 840nm blaze wavelength, Wasatch Photonics, Logan, USA), an achromatic lens and a line scan camera (spl4096-140kmESC, Basler, Ahrensburg, Germany). The overall size of the instrument is quite compact. The sample arm including the fundus camera and wavefront sensing and wavefront correcting part has an extension of 40cm x 50cm x 20cm and is moveable (cf. Fig. 1(B), 1(C)). Currently the AO-OCT reference arm is built on a separate table and has an extension of 60cm x 45cm x 12cm. However, in principle the reference arm can also be incorporated into the moveable instrument head of the sample arm. The spectrometer is separated from sample and reference arm and covers an area of 40cm x 15cm.

The AO-OCT is operated with an A-scan rate of 200kHz, which is translated into a volume acquisition rate of 1.25 volumes per second (2°x2° field of view consisting of 400x365pixels). With the AO-OCT instrument a sensitivity of 86dB was achieved.

2.2 Instrument operation

In order to split the computational workload for data acquisition and wavefront correction, two separate personal computers (PC) are used. One PC is used to operate the AO loop which includes data acquisition from the SH, centroiding, calculation of the wavefront slopes and finally sending the proper commands to the DM to adapt its shape for reducing the wavefront error. This computer is also used to display the images from the anterior segment camera and the AO-fundus camera. Since the amount of data that is acquired using AO-OCT is very

#258577 Received 29 Jan 2016; revised 21 Mar 2016; accepted 1 Apr 2016; published 11 Apr 2016

demanding in terms of RAM memory (~1GB for one 3D data set), a separate PC is used to operate the AO-OCT system. This computer is equipped with a data acquisition card (DAQ) (NI PCI-6115, National Instruments, Austin, USA) and a frame grabber (NI PCIe-1433, National Instruments, Austin, USA). The DAQ card allows to generate the driving signals for the galvanometer scanners and to generate a trigger signal for the line scan camera (the start of each A-scan is triggered). Data from the line scan camera is acquired using the frame grabber. The line camera can be operated at 70kHz with the full line width of 4096 pixels. However, the line rate can be increased by reading fewer pixels. We chose 896 pixels to read out which resulted in an A-scan rate of 200 kHz. Operation and evaluation software of the AO-OCT was developed in LabView (National Instruments, Austin, USA).

2.3 Imaging protocol

Imaging of subjects was done according to the tenets of the Declaration of Helsinki and under a protocol that was approved by the local ethics committee of the Medical University of Vienna. Prior to the measurements informed consent was obtained from all subjects after explaining the form and nature of the measurements. Patients were selected by the Department of Ophthalmology of the Medical University of Vienna. Selection criteria were the ability to fixate and negligible media opacities. The age range of the patients was between 26 and 72 years.

Prior to imaging with the new instrument standard eye examination including infrared reflectance (IR) or fluorescein angiography (FA) fundus imaging was performed. Regions of interest such as lesions or lesion borders were localized on these images and the approximate distances from the fovea were determined to aid the process of finding these lesions with the AO instrument. Each imaging session started with the AO-fundus camera imaging mode. The internal fixation target of the AO-device was then placed in such a way that the prior determined lesion was located within the field of view of the AO-fundus camera. The optimum position of the fixation target was then fine-tuned with the online 4°x4° image of the AO-fundus camera to bring the lesion into the center part of the field of view. Then the focus was adjusted (either to the photoreceptors or to the anterior layers) by changing the shape of the DM and image acquisition was started. For AO-fundus imaging typically 40 frames were recorded, registered to each other [50, 51] and averaged to produce the final AO-fundus image. Depending on the number of regions of interest AO-fundus imaging was performed at several different locations and the corresponding positions of the internal fixation target were saved. After this step the instrument was switched to the AO-OCT imaging mode and AO-OCT volumes were acquired at the same locations as the AO-fundus images. Since the 2°x2° field of view of the AO-OCT is smaller than the field of view of the AO retinal photography (4°x4°), special care was taken that the region of interest was located in the center of the AO-fundus imaging field of view. As a post-processing procedure the recorded AO-OCT B-scans were aligned to each other using cross correlation in order to eliminate artifacts caused by axial eye motion.

3. Results

3.1 Healthy volunteers

In a first step the imaging performance of the instrument was tested in several healthy volunteers. Figure 2 shows representative images recorded with the new instrument in a healthy eye. The large field of view fundus image (cf. Fig. 2(A)) does not show small details as can be seen in the enlarged region (cf. Fig. 2(B)). However the AO-fundus image (Fig. 2(C)) acquired at the same location (temporal = 1°, superior = 2° from the fovea) with the focus set at the photoreceptor layer and showing the same field of view as Fig. 2(B), reveals the photoreceptor mosaic. AO-OCT data is acquired at the central part of the AO-fundus image and provides depth resolved information (Fig. 2(D)). Visualization 1 shows a fly-

#258577 Received 29 Jan 2016; revised 21 Mar 2016; accepted 1 Apr 2016; published 11 Apr 2016

through of AO-OCT B-scans in a linear grey scale. The different retinal layers can be clearly visualized, however, at this retinal location, the separation between end tips of photoreceptors (ETPR) and retinal pigment epithelium (RPE) is not pronounced. Although the focus is set to the posterior layers (bottom part of the images), sufficient signal is obtained from the anterior layers.

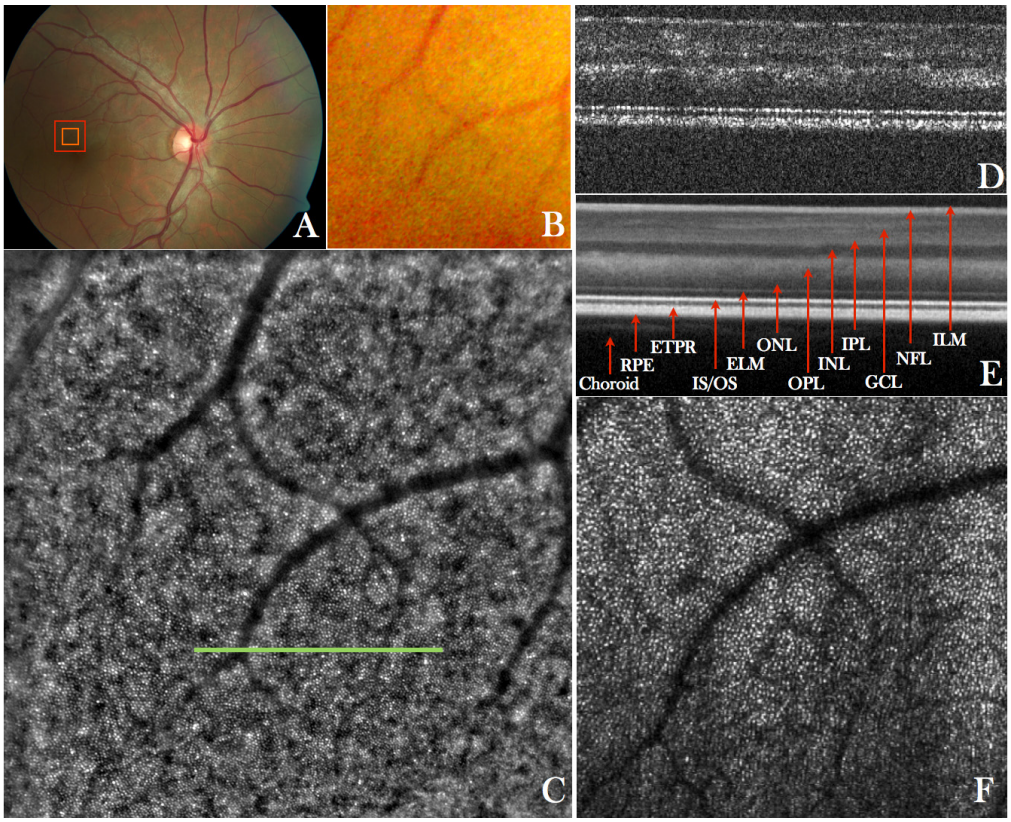

Fig. 2. A) Wide field (50°x50°) standard fundus image of the retina of a healthy volunteer, B) Enlarged region of interest from the wide field image indicated with the red square in A), C) AO-fundus image (4°x4°) acquired with the new instrument at a location indicated with the red square in A)(temporal = 1°, superior = 2°), D) Single B-scan acquired at a location indicated with the green line in C) and extracted from a volume scan (Visualization 1 and Visualization 2) acquired with the AO-OCT mode at a location indicated with the orange square in A), E) Lateral average (corresponding to 0.25°) of 50 B-scans from the volume scan, F) Extracted en-face image from the AO-OCT volume scan by depth integrating over the photoreceptor bands and squaring of the image to display the image on a linear intensity scale.

However, only the posterior layers appear sharp as can be observed by the discrete reflection sites within the junction between inner and outer segments of photoreceptors (IS/OS) and within the ETPR which correspond to individual photoreceptors. For the association of the different posterior layers with anatomical structures we refer to previous work from R. Jonnal et al. [52]. The visualization of individual photoreceptors at this eccentricity from the fovea demonstrates the high transverse resolution that can be achieved with the system.

By averaging 50 B-scans from the volume scan the different retinal layers and structures from the choroid can be seen more clearly. Visualization 2 shows a fly-through of AO-OCT C-scans from the same data set. The movie starts at the anterior layers and shows en-face images of the retina as the coherence plane moves to the posterior part of the retina. Although the focus is still set on the posterior layers, the nerve fiber layer and 3 different layers of

#258577 Received 29 Jan 2016; revised 21 Mar 2016; accepted 1 Apr 2016; published 11 Apr 2016

vasculature can be observed. The cone mosaic can be clearly seen within the IS/OS and at the ETPR layers. The bottom part of the images shows an area that is closer to the fovea. Due to the limited transverse resolution of the system (not the full pupil diameter of 7mm is used) the contrast and visibility of the cone mosaic is reduced in this area. Within the outer segments of cones bright reflection spots can be observed. In previous work we associated these spots with defects within the packing arrangement of the outer segment discs [53]. The images retrieved from the location of the RPE do not show any regular pattern. The en-face projection over the photoreceptor layer shows a similar photoreceptor mosaic as can be seen on the AO-fundus image. However, in the AO-fundus image the mosaic is overlaid with a pattern of relatively large bright and dark patches. Because of the efficient rejection of light that originates from out of the imaging plane using OCT, these are not visible in the AO-OCT images. Figure 3 shows image results obtained at the same location with the focus set to the anterior layers. Visualization 3 shows a fly-through of AO-OCT C-scans. The signal from the anterior layers is now larger than in the previous case (with the focus set to the photoreceptor layers) whereas the signal from the photoreceptor layers is hardly visible. The nerve fiber layer, vessels and small capillaries are imaged sharply and individual nerve fiber bundles can be observed. Three different vasculature beds are present as is shown in Fig. 3. Due to the high collection efficiency of AO assisted systems, the vessels appear with a high image contrast (high signal intensity compared to the surrounding tissue) and can be clearly seen without the need of any motion contrast algorithms [28].

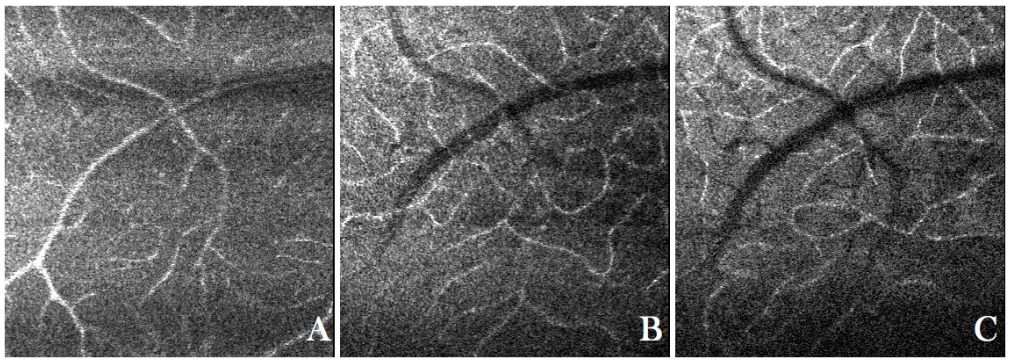

Fig. 3. En-face images of the retina of a healthy volunteer with the focus set to the anterior layers retrieved from an AO-OCT data set. The entire data set can viewed in Visualization 3. A) Vasculature within the ganglion cell layer, B) vasculature within the inner plexiform layer and C) vasculature within outer plexiform layer.

3.2 Patient imaging

The first group of patients that were imaged with the instrument presented Stargardt's disease. Stargardt's disease is a genetic disorder that affects the removal of all-trans-retinol from the photoreceptor, thereby creating hyper-reflective flecks of lipofuscin that build up in the RPE and that lead to a disruption of the photoreceptor layer and RPE. These flecks can be easily observed in autofluorescence images. Figure 4 shows representative images of a patient with Stargardt's disease. The auto fluorescence image (cf. Fig. 4(A)) clearly shows the typical flecks. The high resolution AO-fundus (recorded at location: nasal = 2.3°, inferior = −2.4°) image shows an abnormality on the photoreceptor morphology, density and spacing similar to previous reports [54–56]. Although the flecks are not clearly visible in this imaging modality, a slightly blurred photoreceptor mosaic can be observed at these locations and in the surrounding areas (cf. overlaid manual segmentation). The major part of the image appears sharp. Therefore we do not think that the blurriness is due to errors in the AO correction.

#258577 Received 29 Jan 2016; revised 21 Mar 2016; accepted 1 Apr 2016; published 11 Apr 2016

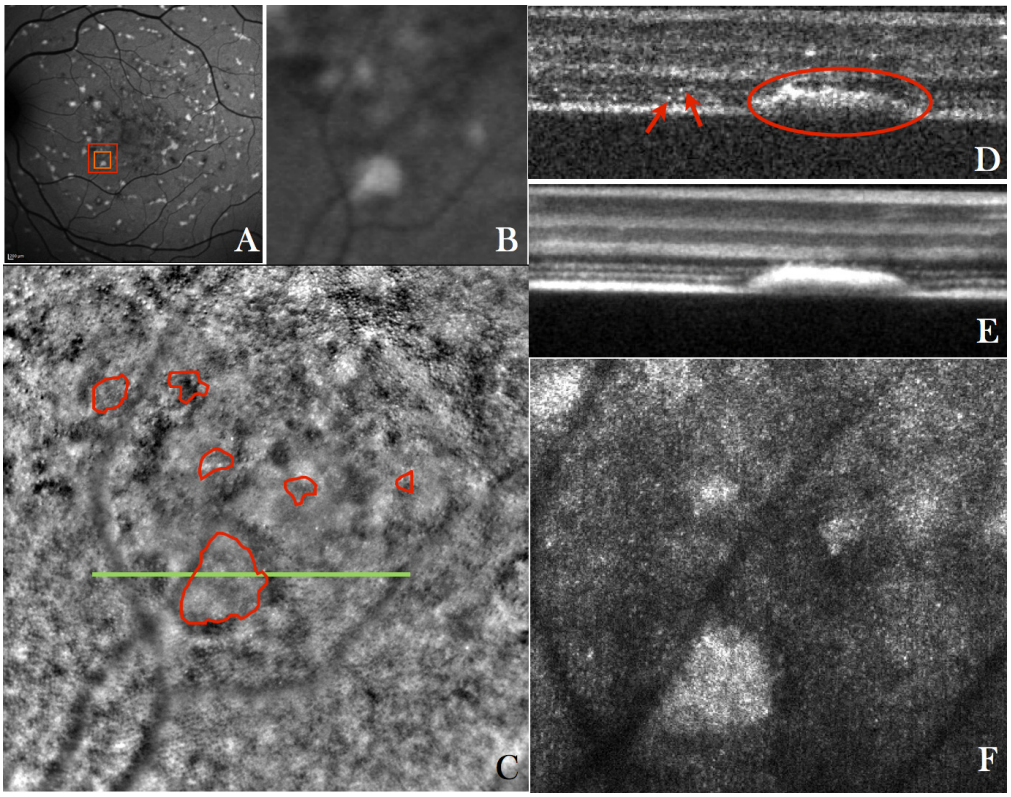

Fig. 4. A) Wide field (30°x30°) autofluorescence fundus image of the retina of a patient with Stargardt's disease, B) Enlarged region of interest from the wide field image indicated with the red square in A) (nasal = 2.3°, inferior = 2.4°), C) AO-fundus image (4°x4°) of the same area as is shown in B) (overlaid in red are the extensions of the flecks that were manually segmented using the AO-OCT data), D) Single B-scan acquired at the location indicated with a green line in C) and extracted from a volume scan (Visualization 4) acquired with the AO-OCT instrument at a location indicated with the orange square in A) (The red arrows indicate the IS/OS junction and ETPR of individual photoreceptors, the red ellipse indicates the extension of a fleck), E) Average of 50 B-scans from the volume scan, F) Extracted en-face image from the AO-OCT volume scan (Visualization 5) by depth integrating over the photoreceptor bands.

The AO-OCT B-scans clearly show the extension of the hyper-reflective flecks through the photoreceptor bands (red ellipse in Fig. 4(D)). In neighboring areas the photoreceptor bands seem to be intact (cf. arrows left hand side of Figs. 4(D)). The B-scans of the entire data set can be viewed in Visualization 4. In some B-scans the two photoreceptors bands and the RPE can be seen. However, as can be observed by visual inspection of the images, the spacing between the individual photoreceptors is larger than in the healthy case (cf. Fig. 2(D)). In addition many B-scans show disruptions in the photoreceptor bands that are probably created by waste deposits (flecks of lipofuscin) that originate from the RPE. Some of these deposits can be even observed in the outer plexiform layer (cf. Fig. 5(A) or frame no. 102 in Visualization 4). These extensions can also be seen in the fly through movie of en-face images (cf. Visualization 5). Interestingly, tiny spots (similar size to the cone photoreceptors) can be observed in the outer nuclear layer (cf. Fig. 5(B) or frame no. 60 of Visualization 5), that are distributed over the entire region. These spots were not found in healthy conditions. At this stage of investigation the anatomical correspondence of these structures is unclear.

#258577 Received 29 Jan 2016; revised 21 Mar 2016; accepted 1 Apr 2016; published 11 Apr 2016

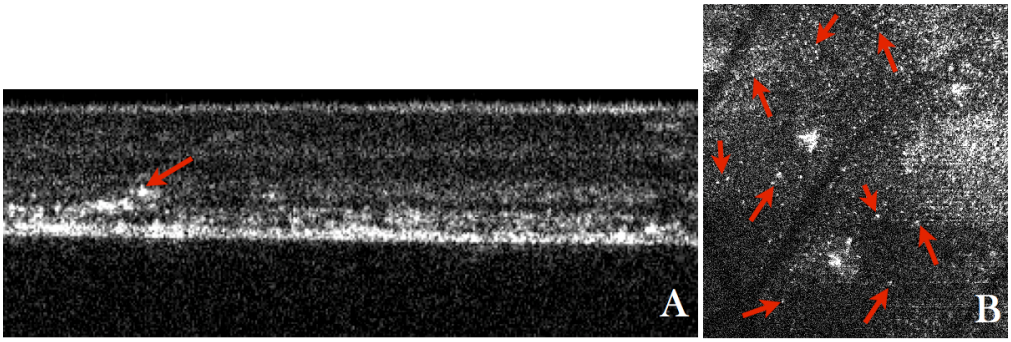

Fig. 5. A) Frame no. 102 from Visualization 4 showing a B-scan where waste deposit within the OPL (indicated with the red arrow) can be observed, B) Frame no. 60 from Visualization 5 showing a depth integrated en-face projection over the OPL where tiny spots with a similar size as cone photoreceptors are observed distributed over the entire image (indicated by the red arrows).

The second group of patients that was imaged with the system presented diabetic disease. Early signs of diabetic retinopathy include bulging of small retinal vessels and capillaries called microaneurysms (MA) that are likely to develop in the inner retinal layers. Beside fundoscopy and color fundus photography, fluorescein angiography is used as the standard approach to visualize MA. A corresponding image is shown in Fig. 6(A). Microaneurysms appear as white dots due to the accumulation of fluorescein in these structures. The AO fundus image (cf. Fig. 6(C)) was recorded with the focus set to the anterior layers. In contrast to an image where the focus is set to the photoreceptor layer (cf. Fig. 2(C)), most vessels appear bright because light from the highly scattering blood constituents and light reflection from the top vessel wall can now be collected by the imaging optics. In general MAs appear as dark roundish structures in the large field of view AO fundus images and show typically weak contrast. This contrast can be greatly increased through AO-SLO imaging with an offset pinhole configuration [57] or through a combination of AO-SLO and fluorescein angiography [58].

High contrast imaging of the MA can also be achieved using AO-OCT. As can be seen in the AO-OCT B-scan (cf. Fig. 6(D)) the MA appears as round shaped structure with a bright reflecting surface and hypo-reflective center. These characteristics can be better observed in the averaged B-scan that is shown in Fig. 6(E) or in the fly through movie of the AO-OCT B-scans that are shown in Visualization 6. Apart from the MA the retina appears normal in this region. It should be noted that the MA causes a shadow on the underlying layers that is most pronounced in the photoreceptor layer. This shadowing effect can be clearly observed in Fig. 7(C) (or frame No. 107 of the en-face movie Visualization 7). As can be seen in Fig. 6(F) the high depth resolution of AO-OCT allows for the visualization of vessel walls in the case of a large vessel (cf. large horizontal vessel in the figure). Another interesting feature that can be observed in the en-face movie is the presence of a large, highly reflecting patch at the inner limiting membrane (cf. Fig. 7(A) or frame No. 14 in Visualization 7). In addition a small vessel loop (possibly a developing MA) can be observed below and next to the large MA (cf. Fig. 7(B) or frame No. 16 in Visualization 7).

#258577 Received 29 Jan 2016; revised 21 Mar 2016; accepted 1 Apr 2016; published 11 Apr 2016

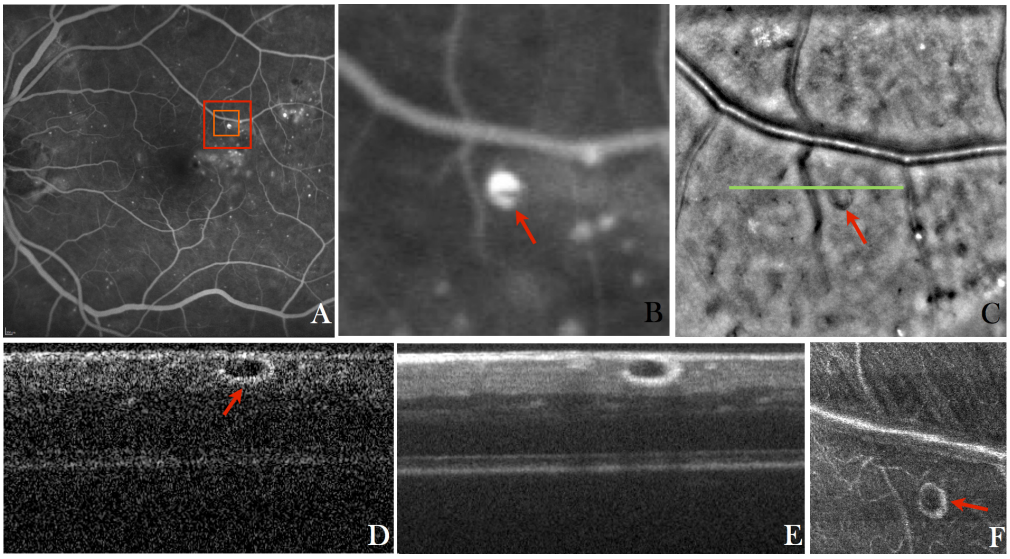

Fig. 6. A) Wide field (30°x30°) fluorescein angiography fundus image of the retina of a patient with diabetic retinopathy, B) Enlarged region of interest from the wide field image indicated with the red square in A), C) AO-fundus image (4°x4°) of the same location as is shown in B), D) Single B-scan acquired at the location indicated with a green line in C) and extracted from a volume scan (Visualization 6) acquired with the AO-OCT instrument at a location indicated with the orange square in A), E) Average of 10 B-scans from the volume scan, F) Extracted en-face image from the AO-OCT volume scan (Visualization 7) by depth integrating over the microaneurysm.

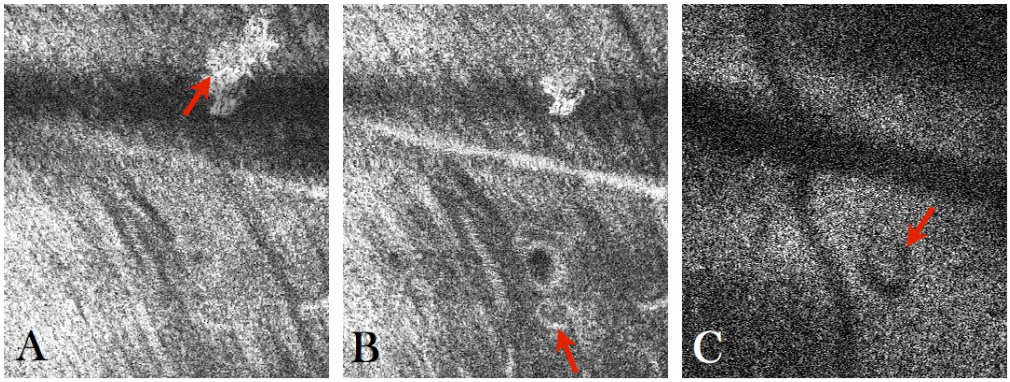

Fig. 7. A) Frame No. 14 from Visualization 7 showing the presence of a large hyper-reflective structure in the nerve fiber layer, B) Frame No. 16 from Visualization 7 where a small vessel loop can be observed, C) Frame No. 107 from Visualization 7 showing the shadowing effect caused by the overlying microaneurysm.

4. Discussion

The compact design and the easy handling of the instrument may facilitate a fast translation of AO-OCT into clinical settings. The field of view (~2°x2°) of our AO-OCT imaging mode is already at the limit although the instrument is operated at 200 kHz A-scan rate. In order to increase the field of view while maintaining the sampling density, the imaging speed has to be further increased at the cost of sensitivity decrease. However, we do believe that the achieved 86dB sensitivity of AO-OCT is already at the lower limit in clinical feasibility. Although imaging speeds of 1MHz have been demonstrated with AO-OCT [33] the sensitivity of such systems is ~7-10dB lower and might be insufficient to obtain satisfying image quality in many patients. One advantage of the current system is its multimodality. In contrast to that a

#258577 Received 29 Jan 2016; revised 21 Mar 2016; accepted 1 Apr 2016; published 11 Apr 2016

stand-alone AO-OCT instrument will have significant drawbacks that are associated with small field of view imaging. Only specific regions of interest such as lesions or borders of lesions can be imaged and identification of these regions during patient alignment will be very difficult. Therefore the combination with an imaging modality that provides a larger field of view, as in our case the AO-fundus camera, is essential to aid and accelerate the alignment procedure. Together with the easy system handling, the operating time for a visit (alignment and imaging) could be kept to minimum. In addition, the relatively large field of view of the AO fundus image greatly facilitates a comparison with other imaging modalities such as standard fundus photography or OCT because specific features of the fundus (such as vessels) can be easily recognized. For this purpose different combinations such as the standard wide field OCT imaging with AO assisted imaging have been proposed earlier and are also feasible [32].

The transverse resolution of the system is limited to ~4µm. Higher resolution can be achieved when a full pupil diameter of ~7mm instead of the 5mm that is supported by the instrument is used. However, such large pupils require excellent wavefront correction (a residual root mean square wavefront error <0.1 over the entire pupil) to get sufficient image quality (i.e. sufficient signal to noise ratio) which might not always be possible in patients. In addition, in some patients the usable pupil diameter is limited to 4-5mm because of age related miosis or the size of the artificial lens that is inserted after cataract surgery. We therefore decided to use a smaller pupil as a compromise between high transverse resolution and wider clinical applicability of the instrument.

Nevertheless there is still some room for improvement. The current system uses a manually operated flipping mirror to switch between the imaging modalities. This is time consuming. Ideally both imaging modes can be operated simultaneously. However, this requires that different wavelengths regions are used for the imaging modalities in order to avoid any cross talk. Another option could be a quasi-simultaneous operation using a fast electronically driven flip-able mirror, which interleaves both modalities. Thereby the read out time of the retinal camera can be used to acquire AO-OCT data. This strategy will also reduce the chances of slight deviations in the alignment during the switching of imaging modalities, which are currently present. In addition, such a system could be used in order to correct for lateral motion as has been proposed for a combination of AO-OCT with AO-SLO [59]. Another issue arises because the system is not equipped with an eye tracker. Thus, motion artifacts may be present in the recorded OCT volume. In order to minimize the influence of these artifacts several volumes are acquired and volumes showing severe motion artifacts are discarded. Although this is time consuming, the implementation of additional hardware that is needed for retinal tracking [32] and the corresponding complexity is avoided. An improved strategy for minimizing motion artifacts may be based on the high B-scan rate of the current system. Thus parts of the entire volume data will not show pronounced artifacts. Motion artifacts may be completely eliminated by recording several volumes within a few seconds and determining those parts of the volume that show no motion artifacts. These may then be merged into one single motion artifact free volume.

Another limitation of the current system is that the reference arm and the spectrometer unit are located at separated breadboards. This increases the overall size of the instrument but with some additional effort both can be merged into the movable instrument table of the sample arm without influencing the overall performance of the instrument. At the moment two computers are used to run the system, which is not ideal for clinical settings. Nevertheless the operation of both imaging modalities may be incorporated into a single computer.

The new system combines two different imaging modalities, which results in complementary data. Especially, the depth information provided by AO-OCT is essential in order to better understand features that are visible in the AO fundus image. When comparing the cone mosaic of a healthy eye using AO fundus imaging and AO-OCT (cf. Fig. 2(C) and 2(F)) a different appearance can be observed (The AO fundus image shows overlaid to the

#258577 Received 29 Jan 2016; revised 21 Mar 2016; accepted 1 Apr 2016; published 11 Apr 2016

cone mosaic bright and dark patches.) The OCT image is generated by integration over the photoreceptor bands. Thus contributions from other layers are completely eliminated. On the other hand, backscattering from all layers may contribute to the AO-fundus image although the signal intensity from these layers will be weighted by the depth of focus of the system. In addition, multiple scattered light, will contribute to the signal in the fundus image while in the case of AO-OCT these light components are greatly attenuated because of the confocal gating. This probably prevents the generation of an AO-OCT image similar to the AO-fundus image by simply integrating the OCT signal over a larger depth. It should be noted, however, that depth integrated AO-OCT images appear very similar to AO-SLO images as has been shown in [25].

The images of patients show the potential of the instrument. For interpretation of patient data the additional information provided by AO-OCT is valuable. For example, the blurred patches which are visible in the fundus image of Stargardt's disease (cf. Fig. 4(C)) are difficult to interpret. However, as can be observed in the AO-OCT data (cf. Fig. 4(F)) these patches correspond to flecks that penetrate the photoreceptor bands. On the other hand, the remaining photoreceptor mosaic appears with higher contrast in the AO-fundus image. In addition to that, AO-OCT reveals structures that might not be observable with any other imaging modality. Such structures are for example the spots within the outer nuclear layer in the patient with Stargardt's disease.

In diabetic patients the contrast of MA in the AO-fundus image is lower than in the AO-OCT images. In fact only the shadow of the MA can be observed in the AO-fundus image. Although the photoreceptors are out of focus, the light which is backscattered from these structures is very large and contributes to the background intensity. In contrast to AO-SLO or AO-OCT, the AO-fundus image is not a confocal imaging modality. Therefore light originating from out of focus planes is not suppressed. Thus other structures that cause shadowing effects (such as microexudates) may appear similar and might be misinterpreted as MA. A clear advantage of AO-OCT is the possibility of a quantitative evaluation of the MA as the volume of these structures can be measured. Details of different MA structures are of great clinical interest as still little is known about MA formation and structural changes over time. Hyper-reflective content within the lumen of MA could be a sign of starting involution. Due to the limited depth resolution of AO-fundus imaging it is very difficult to judge the content of MA because light backscattered from other retinal locations may contribute to the image. Using AO-OCT these contributions can be completely eliminated and the content can be determined.

5. Conclusion

We presented a new user friendly, multi-modal adaptive optics imager that combines AO fundus imaging and AO-OCT in a single instrument with compact design. First imaging results in healthy volunteers and patients are promising. The instrument design facilitates an easy translation of the system into clinical settings.

Acknowledgements

Financial support from the European project FAMOS (project number FP7 ICT 317744) and the Macular Vision Research Foundation (MVRF, USA) is acknowledged. We thank Boris Hermann, Abhishek Kumar, Mengyang Liu and Daniel Fechtig from the Center for Medical Physics and Biomedical Engineering at the Medical University of Vienna for their support and fruitful discussion.

#258577 Received 29 Jan 2016; revised 21 Mar 2016; accepted 1 Apr 2016; published 11 Apr 2016